

Thermal Study of Photovoltaic Embedded Hollow Concrete Block

Abbas S. Toufaily¹, Rida Nuwayhid^{1,*}, Fadi Moucharrafi², Bechara Nehme³,
Elias Farah⁴, Marc A. Rosen⁵

¹Department of Mechatronics Engineering, Faculty of Engineering and Computer Science,
American University of Science and Technology (AUST), Lebanon

²Department of Architecture, School of Architecture and Design, Holy Spirit University of Kaslik (USEK), Lebanon

³Department of Electrical, Telecom and Computer Engineering, School of Engineering, Holy Spirit University of Kaslik (USEK),
Lebanon

⁴Department of Civil Engineering, School of Engineering, Holy Spirit University of Kaslik (USEK), Lebanon

⁵Faculty of Engineering and Applied Science, Ontario Tech University, Canada

Received September 29, 2025; Revised December 26, 2025; Accepted January 20, 2026

Cite This Paper in the Following Citation Styles

(a): [1] Abbas S. Toufaily, Rida Nuwayhid, Fadi Moucharrafi, Bechara Nehme, Elias Farah, Marc A. Rosen, "Thermal Study of Photovoltaic Embedded Hollow Concrete Block," *Civil Engineering and Architecture*, Vol. 14, No. 2, pp. 840 - 857, 2026. DOI: 10.13189/cea.2026.140213.

(b): Abbas S. Toufaily, Rida Nuwayhid, Fadi Moucharrafi, Bechara Nehme, Elias Farah, Marc A. Rosen (2026). *Thermal Study of Photovoltaic Embedded Hollow Concrete Block*. *Civil Engineering and Architecture*, 14(2), 840 - 857. DOI: 10.13189/cea.2026.140213.

Copyright©2026 by authors, all rights reserved. Authors agree that this article remains permanently open access under the terms of the Creative Commons Attribution License 4.0 International License

Abstract This study presents the Photovoltaic Hollow Concrete Block (PVHCB), a novel building-integrated photovoltaic (BIPV) system that integrates a thin photovoltaic film within the internal cavity of a standard hollow concrete block. The proposed block configuration consists of an external transparent and/or translucent layer that permits the transmission of incident solar radiation to the embedded photovoltaic element, coupled with a conventional opaque concrete inner layer that preserves the structural and thermal characteristics required for building envelopes. Thermal resistance network models are developed to evaluate heat transfer through the PVHCB, from which U-values are derived for various hollow concrete block geometries and material configurations. To enable location-specific performance assessment, a simple, universally reproducible methodology for generating solar radiation data is adopted, allowing the creation of representative seasonal solar profiles for Beirut, Lebanon. These data are subsequently used to analyze the transient thermal behavior of a south-facing wall constructed from insulated PVHCB units under seasonal operating conditions. Detailed energy balance equations are employed to estimate the temperature distribution within the block and the operational conditions of the photovoltaic

film. The results suggest that a 20 m² south-facing PVHCB wall in Beirut could generate between 794 W (39.7 W/m²) and 846 W (42.3 W/m²) of electrical power, depending on seasonal variations and thermal conditions. Although the present investigation is preliminary and does not yet address mechanical performance, economic feasibility, or long-term material durability, the findings demonstrate the PVHCB's potential to function simultaneously as a structural building component and a supplementary on-site power generation system, thereby contributing to the development of sustainable and energy-efficient building envelopes, particularly in detached rural homes.

Keywords Building, Integrated, Photovoltaics, Hollow, Concrete, Block, Photovoltaic, Thermal, Transient, Solar, Energy, Power

1. Introduction

The need to address climate change and reduce reliance on fossil fuels for power generation has motivated the investigation of renewable energy technologies. A new

paradigm has started to emerge in the building sector that aims for a dual, space-saving benefit by using construction materials and components that also generate electrical power for occupants.

When the available renewable energy source is solar, the energy conversion task can be accomplished by direct energy conversion devices that convert solar energy to electricity. This can be achieved most appropriately by employing either thermoelectric or photovoltaic devices.

Thermoelectric generators (TEG's) convert heat to electricity directly at efficiencies that, although improving with research, currently do not exceed about 10% [1]. The value of using TEG's in building wall energy harvesting is that they are heat-driven and only require a temperature difference. Jabri et al [2] pointed this out by comprehensively examining thermoelectric conversion in buildings. On the other hand, there have been only a few studies on TEG-embedded hollow concrete blocks (HCB's), the most notable being that of Wehbe et al [3], which developed a mathematical model and indicated a possibility to tailor wall-incorporated TEG's to produce a required output power load for a dwelling.

Photovoltaic (PV) systems, on the other hand, have reached efficiencies of over 20% and have emerged as a viable option due to their market availability, sustainability, and declining cost of implementation. However, the integration of PV modules into building components requires innovation beyond traditional installation.

The traditional role of buildings has historically been to provide shelter as well as thermal comfort for dwellers. Recently however, buildings have started to evolve into cogenerating systems – providing both thermal conditioning as well as electrical output. On the thermal side, the Trombe wall (TW) is a convenient building wall element that can provide winter heating as well as summer ventilation. Bevilacqua et al [4] studied the performance of a TW in a building and reported reduced heating and cooling energy requirements in a Mediterranean climate. In fact, the TW wall presents a very convenient and protected method for incorporating PV films on a building façade.

Sirin et al [5] published a comprehensive review of building-integrated photovoltaic systems (BIPV) as well as BIPV/thermal systems and concluded that they offer a very promising route for advancement. Liu et al [6] focused on wall-integrated solar energy technologies (WISE), which encompass sun-spaces, PV-Trombe walls, as well as solar PV-thermal systems. Ma et al [7] published a comprehensive critical review of various technologies that can be adapted to BIPV-thermal systems.

In fact, BIPV systems represent a significant advancement in sustainable architecture and, as such, several companies have introduced products that merge energy generation with construction materials. For example, Mitrex's "Solar Brick" panels offer a modular double-leaf cladding brick-stone option that incorporates PV elements within facade systems [8]. These innovations demonstrate how PV systems can be adapted into

construction units, while maintaining rigidity and opacity [9], [10].

Beyond visual integration, recent research has explored thermally responsive and multi-functional building blocks. Studies on BIPV applications highlight the challenge of balancing power generation with thermal insulation and structural integrity [11]. This trade-off becomes more critical in regions with large seasonal temperature variations [12].

While various studies discuss BIPV systems and the thermal behavior of PV modules, to the best of the authors' knowledge, no previous work has directly investigated the integration of photovoltaic films inside a translucent Hollow Concrete Block (HCB), nor has it modeled its transient thermal response using customized geometric configurations. The PVHCB system proposed in this study introduces a novel paradigm by embedding photovoltaic material within a structurally and thermally functional concrete building block that includes a translucent outer layer. Additionally, in order to develop building wall elements that transmit sufficient light, translucent or even transparent materials are needed. In fact, there are a few studies that suggest translucent materials can be made that may have reasonable structural and optical properties [13].

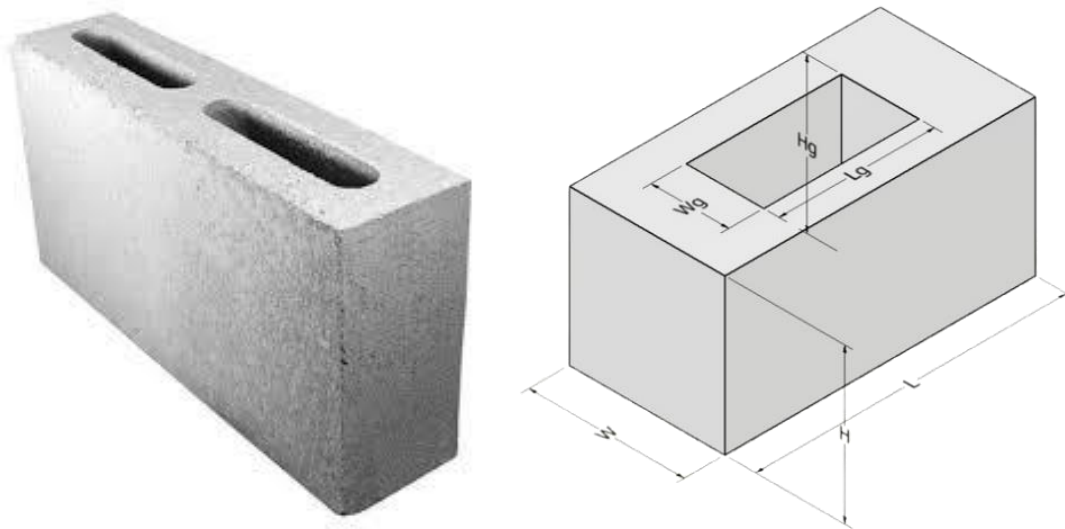
The objectives of this work are: to introduce the PVHCB as a candidate half-light transmitting/ half regular concrete building block; to assess the effect of geometry on the thermal resistance of regular HCB's as well as PVHCB's; to present an outline of an appropriate solar data generation methodology; to evaluate the transient thermal response of HCB's and PVHCB's when exposed to insolation; and to estimate the power generation potential of insulated PVHCB's.

2. Materials and Methods

The integration of PV technology into construction materials offers a promising path toward energy-efficient buildings. While most Building-Integrated Photovoltaic (BIPV) systems rely on surface-mounted detached modules, this study proposes a novel concept: The Photovoltaic Hollow Concrete Block (PVHCB), which embeds a photovoltaic film on the internal cavity(s) of a hollow concrete block similar to the one shown in Fig. 1. The resulting PVHCB features a transparent or translucent outer layer, to enable solar transmission, and a regular concrete inner layer to maintain structural integrity and sufficient thermal mass. Analytical thermal resistance models and transient energy simulations are developed to evaluate the system's performance under both winter and summer typical conditions in Beirut. Under specified solar insolation levels, temperatures are calculated for regular HCB's as well as for the PVHCB's outer surface and its inner interface. The study highlights the trade-off between thermal insulation and electrical efficiency, offering a new prospect in sustainable building technologies.

Fig. 2a shows a top view of the proposed PVHCB concept applied to a 20 cm-wide block. The outer layer consists of a semi-transparent building material such as translucent concrete (TC), while a robust photovoltaic film is embedded on the interior face of the TC, allowing for a vertical cooling gap between it and the inner lightweight regular concrete (RC). As shown in the side view in Fig. 2b, the internal cavities of stacked open-hollow PVHCB units

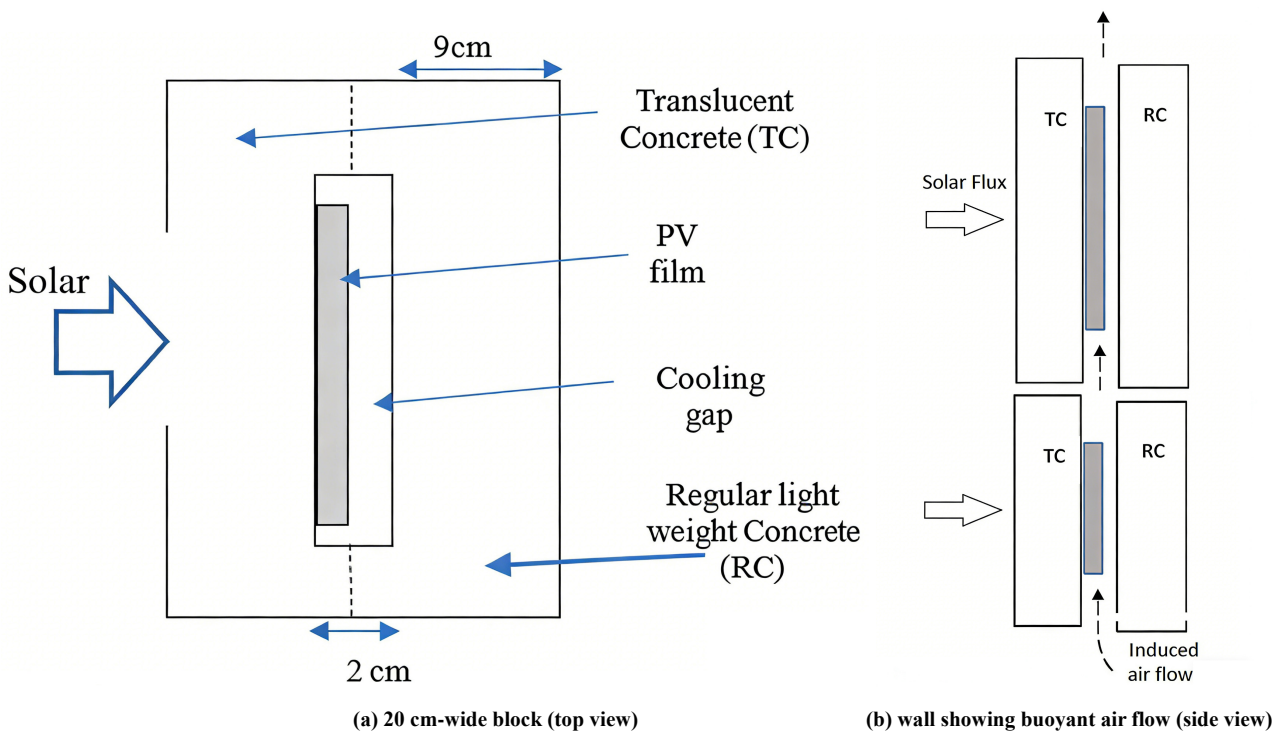
may be aligned vertically to promote a natural upward air draft promoting natural convective cooling. To compensate for the possible load imbalance caused by using dense translucent concrete on one side, lightweight concrete, with the added benefit of higher thermal insulation than the regular concrete block work, may be adopted in the inner layer to maintain structural balance and ease of handling – a solid mechanics study of this issue is a future project.



(a) two-hollow central gap

(b) HCB geometrical design

Figure 1. Typical local HCB



(a) 20 cm-wide block (top view)

(b) wall showing buoyant air flow (side view)

Figure 2. PVHCB block and wall concepts

As a region with little energy resources and poor building regulations, while at the same time being blessed with ample solar sunshine most of the year, Beirut, Lebanon presents an interesting paradigm of buildings and energy Mediterranean climate. In Lebanon, external walls are typically constructed using hollow concrete blocks, most often measuring 20 cm × 20 cm × 40 cm (height × width × length), although narrower 20 cm × 10 cm × 20 cm blocks are sometimes used in double leaf walls. With blocks being the basic unit of wall construction, it is worthwhile to study their thermal behavior. Other than the investigation of the specific concrete mixture used in the fabrication of the block and the material chosen to fill its cavities, the overall geometric configuration of the block itself is worth studying as these impacts building wall heat transfer [14].

The study starts with the steady-state thermal analysis of regular hollow concrete blocks in a Beirut climate. Hence, U-value calculations for various geometric configurations of regular HCB's are presented. The introduced hypothetical PVHCB's steady-state U-values are then estimated using Beirut ambient temperature data. Following that, a detailed and easily adaptable section on solar data generation methodology is presented with a specific application to Beirut.

Rather than using estimated sol-air temperatures for the exposed south walls, this work uses exact and detailed generated solar monthly and hourly radiation data as input. The transient thermal behaviors of regular HCB's as well as for the proposed PVHCB's are presented and discussed. Finally, the theoretical hourly and monthly averaged power output per unit of insolated south wall area, constructed from PVHCB units and exposed to representative winter and summer conditions in Beirut, is estimated.

3. HCB Steady Thermal Analysis

The simplified model of the regular HCB is designed as a rectangular solid building block featuring a centrally positioned rectangular cavity. The block's geometry is defined by its length L , height H , and width W , while the cavity is symmetrically located with dimensions proportional to those of the block. The length of the gap is denoted L_g , its width W_g , and its height H_g as shown in Fig. 1b.

The steady thermal analysis of the HCB considers 1-dimensional heat conduction through the solid concrete material, while heat transfer in the central air gap is taken

to be conduction effectively. The 1-D analysis is justified in this scoping design study by the fact that the thermal driving force (the greatest ΔT) is between the outside and inside surfaces of the block, which is part of a tall wall. This is true in both summer and winter, especially if the dwelling is conditioned [15]. Additionally, convection heat transfer occurs at the inner and outer block face surfaces. The thermal performance of the block is characterized through the calculation of thermal resistance components and the determination of the overall heat transfer coefficient (U-value: the thermal transmittance coefficient). The analysis investigates the influence of geometric parameters, material properties, and boundary conditions on the overall thermal resistance and heat transfer efficiency of the block.

The electrical resistance model in Fig. 3 serves as an analogy for the thermal resistances in the HCB. The edge resistances R_{edge} are represented by R_1 and R_3 , while the mid-section resistance R_{mid} is represented by R_2 . These three resistances are thermally-connected in parallel.

Fig. 3 illustrates the detailed thermal resistance network of the hollow concrete block with a centered rectangular internal gap (cavity). Heat flows from the ambient temperature T_a to the inner surface temperature T_{in} through three parallel paths: two edge paths and one central (mid) path. Each path includes convective resistances on the inner and outer surfaces ($R_{conv,in}$, $R_{conv,out}$) and conductive resistances through the block material (R_{cond} , $R_{cond,edge}$). The mid path also includes a gap resistance R_{gap} , representing heat flow through the internal cavity, which is modeled as effective conduction.

The total heat transfer coefficient (U-value) is given by:

$$U = \frac{1}{R_{total}} = \frac{1}{R_{mid}} + \frac{2}{R_{edge}} \quad (1)$$

Four geometric configurations of a hollow concrete block are analyzed to evaluate their thermal performances: a fixed-gap configuration with predefined length and width fractions, a flexible model that allows user-defined length and width fractions, an advanced model enabling customization of length, width, and height fractions of the internal gap, and a hybrid configuration composed of half-glass and half-concrete material with full customization of the gap dimensions.

For each model, the thermal resistance components and the overall heat transfer coefficient are calculated using Equation (1). Additionally, an interactive Excel-based tool is developed for each configuration to facilitate user input and to streamline the analysis process.

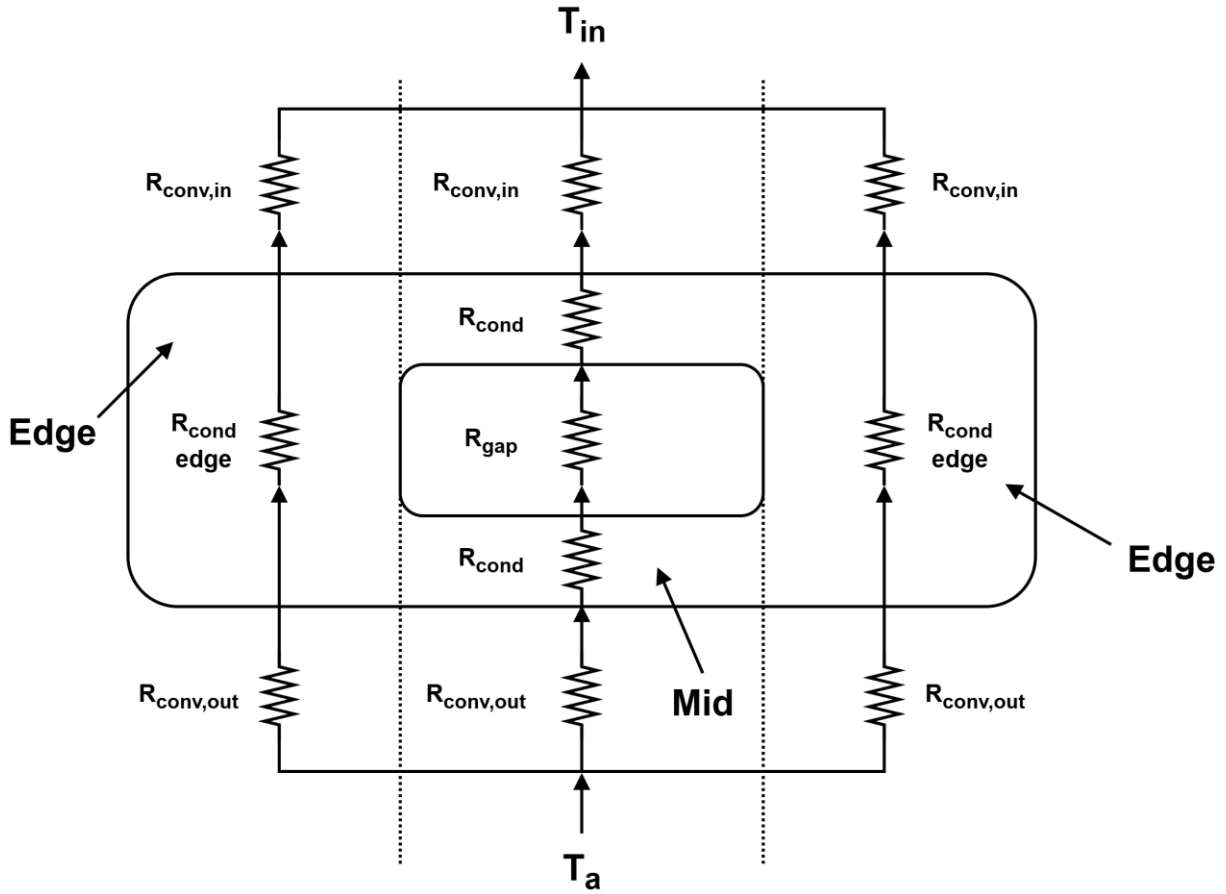


Figure 3. Thermal resistances network for hollow concrete block

3.1. Model 1: HCB with Centered Rectangular Gap

This model considers the HCB to have a fixed rectangular gap centrally positioned within the block. The dimensions of the gap are defined such that its length is equal to one half of the total length of the block $L/2$, and its width is equal to half of the total width of the block $W/2$. The component thermal resistance and the overall heat transfer coefficient (U -value) of the HCB (in W/m^2K) are as follows:

$$R_{mid} = \frac{A_{total}(k_c k_{gap} h_i + \frac{W}{2} h_i k_{gap} h_o + \frac{W}{2} h_i k_c h_o + h_o k_c k_{gap})}{h_i k_c k_{gap} h_o A_1} \quad (2)$$

where

- h_i : Internal heat transfer coefficient (W/m^2K)
- h_o : External heat transfer coefficient (W/m^2K)
- k_c : Thermal conductivity of concrete (W/mK)
- k_{gap} : Thermal conductivity of the gap (W/mK)
- W : Width of HCB (m)
- L : Length of HCB (m)
- H : Height of HCB (m)

Similarly, R_{edge} is given by

$$R_{edge} = \frac{A_{total}(k_c h_i + W h_o h_i + h_o k_c)}{h_o h_i k_c A_2} \quad (3)$$

Finally, from Equation (1), the U -value is found to be

$$U = \frac{h_o h_i k_c (k_{gap} A_1 D_2 + 2 A_2 D_1)}{A_{total} D_1 D_2} \quad (4)$$

where

$$D_1 = k_c k_{gap} h_i + \frac{W}{2} h_i k_{gap} h_o + \frac{W}{2} h_i k_c h_o + h_o k_c k_{gap} \quad (5)$$

$$D_2 = k_c h_i + W h_o h_i + h_o k_c \quad (6)$$

3.2. Model 2: HCB with Variable Length and Width

The second model introduces an HCB with a flexible rectangular gap, allowing the user to specify the gap dimensions as a fraction of the block’s total length and width. In this model, the length of the gap L_g is defined as a fraction of the total length L such that $L_g = fL$, while the width of the gap W_g is determined by a fraction of the total width W such that $W_g = gW$. This approach offers flexibility in analyzing the thermal performance of the block by the ability to vary the proportions of the gap. The values of both f and g are kept within the range of 0.1 to 0.75 to ensure realistic and practical configurations. The objective remains to determine the thermal resistance components and the overall heat transfer coefficient (U -value) while assessing how changes in gap dimensions influence the thermal insulation characteristics of the block.

For model 2, R_{mid} is given by

$$R_{mid} = \frac{A_{total}(k_c k_{gap} h_i + (W - gW) h_i k_{gap} h_o + gW h_i k_c h_o + h_o k_c k_{gap})}{h_i k_c k_{gap} h_o f L H} \quad (7)$$

while R_{edge} is given by

$$R_{edge} = \frac{A_{total}(2k_c h_i + 2W h_o h_i + 2h_o k_c)}{h_o h_i k_c (L - fL) H} \quad (8)$$

Here, the U -term is given by

$$U = \frac{h_o h_i k_c (k_{gap} f L H D_2 + 2(L - fL) H D_1)}{A_{total} D_1 D_2} \quad (9)$$

where D_1 and D_2 are now given by

$$D_1 = k_c k_{gap} h_i + (1 - g) W h_i k_{gap} h_o + gW h_i k_c h_o + h_o k_c k_{gap} \quad (10)$$

$$D_2 = 2k_c h_i + 2W h_o h_i + 2h_o k_c \quad (11)$$

3.3. Model 3: HCB with Variable Length, Width, and Height

The third model of the HCB allows an adjustable rectangular gap size, providing the ability to specify the gap's dimensions in terms of length, width, and height. In this model, the length of the gap and the width are as specified in the previous model, with the introduction of the new hyperparameters relating to the gap height-to-HCB height, which is given as $H_g = sH$. The values of f , g , and s are kept within the range 0.1 to 0.75 to ensure practical, robust and realistic configurations. The thermal resistance components and the overall heat transfer coefficient (U-value) are now found, allowing the investigation of how changes in the gap's length, width, and height influence the thermal insulation properties of the block. In this most general model,

$$R_{mid} = \frac{A_{total}(k_c k_{gap} h_i + (W - gW) h_i k_{gap} h_o + gW h_i k_c h_o + h_o k_c k_{gap})}{h_i k_c k_{gap} h_o f L s H} \quad (12)$$

$$R_{edge} = \frac{A_{total}(2k_c h_i + 2W h_o h_i + 2h_o k_c)}{h_o h_i k_c (L - fL) H} \quad (13)$$

Finally, from Equation (1), the U -term is given by

$$U = \frac{h_o h_i k_c (k_{gap} f L s H D_2 + 2(L - fL) H D_1)}{A_{total} D_1 D_2} \quad (14)$$

Where

$$D_1 = k_c k_{gap} h_i + (1 - g) W h_i k_{gap} h_o + gW h_i k_c h_o + h_o k_c k_{gap} \quad (15)$$

$$D_2 = 2k_c h_i + 2W h_o h_i + 2h_o k_c \quad (16)$$

3.4. Evaluation of Total Thermal Resistance for HCB Configurations

Fig. 4 illustrates the effect of the geometric hyperparameters on the total thermal resistance R_{tot} of the Hollow Concrete Block unit. The horizontal axis

represents the length fraction of the embedded air gap f , while each curve corresponds to a fixed value of the width fraction g , representing the proportion of the total block width occupied by the internal gap.

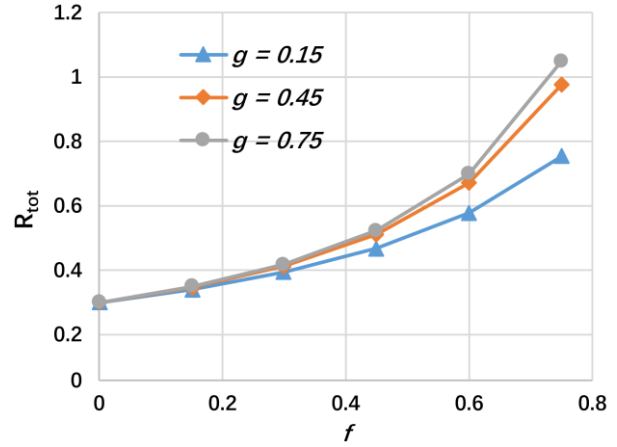


Figure 4. Effect of gap length fraction f and width fraction g on total thermal resistance of HCB

As the gap length fraction f increases, R_{tot} rises nonlinearly, indicating an enhancement in thermal insulation due to the reduced effective conduction path. Additionally, at higher values of g , the rate of increase in R_{tot} is more pronounced. This suggests that both the extension of the gap in length and its widening play significant roles in attenuating heat transfer across the block. These trends emphasize the importance of internal geometry optimization on the thermodynamic design of PV-integrated building components, enabling passive thermal control without compromising structural integrity. For $f \rightarrow 0$ for any g , $R_{tot} \approx 0.3 \text{ m}^2\text{K/W}$, which is consistent with Moucharrafi et al's value of $0.292 \text{ m}^2\text{K/W}$ [16].

3.5. Hybrid Glass-Concrete HCB (HGCB) with Variable Length, Width, and Height

This calculational model introduces a hybrid Hollow Concrete Block (HGCB) configuration, in which the outer half of the block is constructed from transparent glass, while the inner half remains concrete, as shown in Fig. 5. This design allows light transmission through the outer surface—a feature that is particularly advantageous when the inner gap may be used to house a photovoltaic layer. The block retains a centrally located rectangular air gap, whose dimensions are adjustable using the same fractional parameters as in the third model. In this section, neither capacitance effects nor the transmissivity of the outer layer is of concern since only steady resistance parameters are considered in this section. The effect of transmissivity and heat capacity will be considered in the transient analysis in sections 5.1 and 5.2.

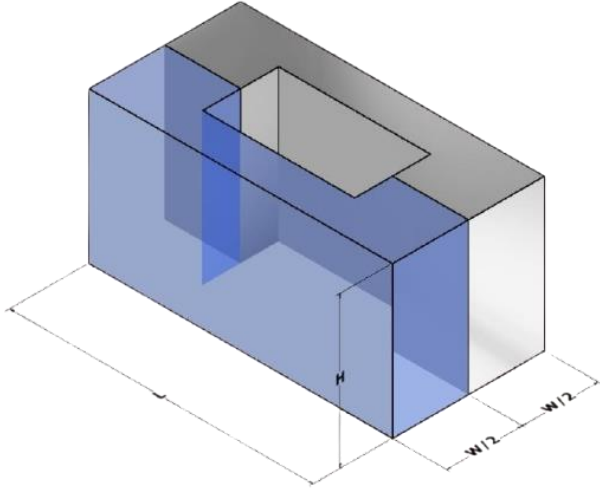


Figure 5. Conceptual Half-Glass Half-Concrete HCB (HGCB)

In this configuration, heat conduction occurs through both the glass and concrete layers, with differing thermal conductivities accounted for in the resistance analysis. The thermal resistance components are reformulated accordingly, and the overall heat transfer coefficient (U-value) is recalculated to reflect the new material components.

R_{mid} and R_{edge} are given by

$$R_{mid} = \frac{D_1}{2fsh_ik_c k_{glass} k_{gap} h_o} \quad (17)$$

$$R_{edge} = \frac{D_2}{2(1-f)h_o h_ik_c k_{glass}} \quad (18)$$

The U-term is given by

$$U = \frac{2h_o h_ik_{glass} k_c (k_{gap} f s D_2 + (1-f) D_1)}{D_1 D_2} \quad (19)$$

where

$$D_1 = 2k_c k_{glass} k_{gap} (h_i + h_o) + Wh_i h_o [(1-g)(k_{gap} k_c + k_{glass} k_{gap}) + 2gk_{glass} k_c] \quad (20)$$

$$D_2 = 2gk_{glass} k_c (h_i + h_o) + Wh_i h_o (k_{glass} + k_c) \quad (21)$$

Fig. 6 shows that as the gap occupies a larger share of the block length (f increases from 0 to 0.75), the overall thermal resistance R_{tot} increases for any gap-width setting, confirming that lengthening the insulating air channel hinders heat flow. Up to about $f \approx 0.4$, the three curves are almost identical, indicating that when the gap is still short, its width ($g = 0.25, 0.50, 0.75$) has little influence—conduction through the surrounding glass-concrete still dominates. Beyond $f \approx 0.6$, however, the curves separate: the widest gap ($g = 0.75$) shows the steepest rise, while the narrowest ($g = 0.25$) gives the lowest R_{tot} . This divergence suggests that once the air channel is long enough for convection to be largely suppressed, widening it further adds a significant extra resistance, making the mixed glass-concrete block most effective thermally when both the gap length and width fractions are high.

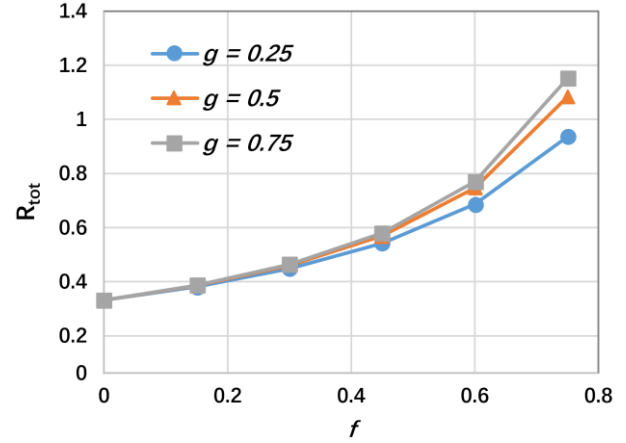


Figure 6. Effect of gap length fraction f and width fraction g on total thermal resistance of half-glass/half-concrete HCB

4. Solar Energy Data Generation

The use of proper, location-specific, solar radiation data is important. In this work, the generation of solar data for Beirut is outlined. This includes monthly average daily radiation and average hourly radiation for the representative day of each month. These determinations are based on a set of standard correlations and equations as presented in Duffie and Beckman [17]. As insolation data for typical summer as well as winter months in coastal Lebanon are not readily available, this work may provide an accurate and consistent set of solar data for further research.

4.1. Monthly Average Daily Solar Data

Initially, radiation data on a horizontal surface using Page's empirical correlation is considered. Then the model is extended to tilted surfaces using the isotropic sky model.

Page's correlation provides a well-established and simple method for relating extraterrestrial solar data to solar data at a particular terrestrial location with a specific climate by the use of climatic constants as well as daylengths for the closest known terrestrial station (see equation 26 below). The method below starts with knowledge of the solar declination for the time of the year, which is a seasonally dependent global attribute. The Solar declination angle δ is computed for the average day of each month using:

$$\delta = 23.45 \sin\left(\frac{360(284+n)}{365}\right) \quad (22)$$

where n is the Julian day.

To find the duration of sunlight, the day length, the sunset hour angle w_s is calculated as

$$w_s = \cos^{-1}(-\tan\phi \tan\delta) \quad (23)$$

where Beirut is at a latitude of approximately $\phi = 34^\circ$.

Using the sunset hour angle, the day length N is

computed:

$$N = \frac{2}{15} w_s \tag{24}$$

The extraterrestrial solar radiation on a horizontal surface, \bar{H}_o , is calculated next. This value represents the theoretical solar radiation received at the top of the atmosphere on a horizontal surface:

$$\bar{H}_o = \frac{24 \times 3600 G_{sc}}{\pi} \left(1 + 0.033 \cos\left(\frac{360n}{365}\right) \right) \left(\cos\varphi \cos\delta \sin w_s + \frac{\pi w_s}{180} \sin\varphi \sin\delta \right) \tag{25}$$

where $G_{sc} = 1367 \text{ W/m}^2$ is the solar constant for Earth outside the atmosphere.

The monthly average daily global radiation on a horizontal surface at ground level is then estimated using Page’s correlation. This empirical model relates the clearness index to the ratio of sunshine duration:

$$\frac{\bar{H}}{\bar{H}_o} = a + b \left(\frac{\bar{n}}{\bar{N}} \right) \tag{26}$$

where \bar{H} is the monthly average daily global radiation on a horizontal surface, \bar{n} is the average actual sunshine duration, and a and b are empirical climatic coefficients.

Fig. 7 shows a comparison between the radiation values estimated using Page’s correlation and those obtained from PVGIS [18] – a satellite-based source of coarse solar data. The shape of the curve and the closeness of the data points support the validity of using Page’s correlation with the selected a and b values for locations like Beirut, where local sunshine duration and climatic patterns align well with the assumptions of the model. This confirms that

Page’s correlation can serve as a practical and reasonably accurate tool for estimating horizontal surface radiation when satellite or ground measurement data are unavailable or not detailed sufficiently.

4.2. Monthly Average Hourly Solar Data

After computing the monthly average daily solar radiation for an entire year, the next step involved estimating the average hourly solar radiation for two representative months—January and July. Initially, the monthly average hourly radiation was derived from the daily average values using the Collares-Pereira and Rabl (CPR) correlation model [17]:

$$r_t = \frac{\bar{I}}{\bar{H}} \tag{27}$$

where

\bar{I} : monthly average hourly radiation

\bar{H} : monthly average daily radiation

Thus,

$$r_t = \frac{\pi}{24} (a + b \cos w) \frac{\cos w - \cos w_s}{\sin w_s - \frac{\pi w_s}{180} \cos w_s} \tag{28}$$

$$a = 0.409 + 0.5016 \sin(w_s - 60) \tag{29}$$

$$b = 0.6609 - 0.4767 \sin(w_s - 60) \tag{30}$$

Subsequently, the factor R_b , which accounts for the geometric relationship between the tilted and horizontal surfaces, is calculated:

$$R_b = \frac{\cos\theta}{\cos\theta_z} = \frac{\cos(\varphi - \beta) \cos\delta \sin w + \sin(\varphi - \beta) \sin\delta}{\cos\varphi \cos\delta \sin w + \sin\varphi \sin\delta} \tag{31}$$

where w is the solar hour angle.

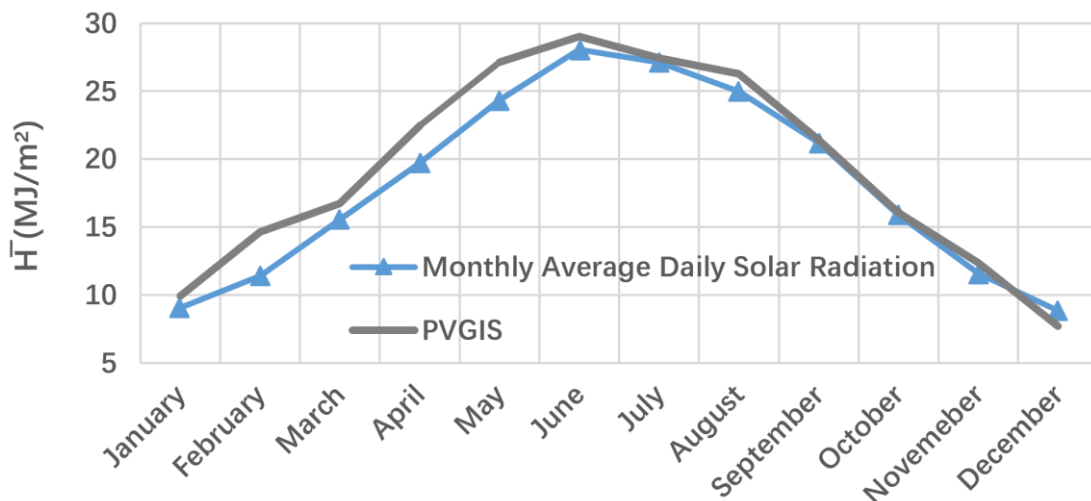


Figure 7. Monthly averaged horizontal solar radiation in Beirut (2025)

The extraterrestrial monthly average hourly radiation on a horizontal surface \bar{I}_0 is computed as:

$$\bar{I}_0 = G_{sc} \left(1 + 0.033 \cos \frac{360n}{365} \right) (\cos \phi \cos \delta \cos \omega + \sin \delta \sin \phi) \quad (32)$$

Next, the clearness index k_t is determined to evaluate the atmospheric transparency at the site:

$$\bar{k}_t = \frac{\bar{I}}{\bar{I}_0} \quad (33)$$

Finally, applying the isotropic sky model, the hourly solar radiation on a tilted surface \bar{I}_T is computed:

$$\bar{I}_T = \bar{I}_b R_b + \bar{I}_d \left(\frac{1 + \cos \beta}{2} \right) + \bar{I} \rho_g \left(\frac{1 - \cos \beta}{2} \right) \quad (34)$$

where

\bar{I}_T : monthly average hourly solar radiation on a tilted surface

\bar{I}_b : monthly average hourly beam radiation on a horizontal surface

\bar{I}_d : monthly average hourly diffuse radiation on a horizontal surface

\bar{I} : monthly average hourly radiation on a horizontal surface

β : surface tilt angle

ρ_g : ground reflectance

The monthly average solar radiation is evaluated for Beirut for the representative months of January (winter) and July (summer), using a surface tilt angle 90° representing a vertical wall. The analysis is carried out over a day time span of 7:00 a.m. to 7:00 p.m.

Summer and winter hourly radiation for horizontal and vertical surface in Beirut is shown in Fig. 8. The results show that although horizontal radiation in July (the sun is at its most direct solar intensity on the 22nd of June since the solar altitude angle at 12 hours noon time at its highest impact on horizontal and south wall vertical plane in Lebanon) reaches significantly higher peak values—exceeding 900 W/m^2 around noon—the tilted surface receives more consistent solar input across the day in January, particularly during midday hours. This highlights the seasonal variation in solar incidence angles, where vertical surfaces perform better in winter, while horizontal surfaces dominate in summer due to the sun's higher elevation. Additionally, the longer daylight duration in July results in a broader radiation curve, contributing to greater total daily energy potential despite a slightly lower tilted-surface peak compared to January.

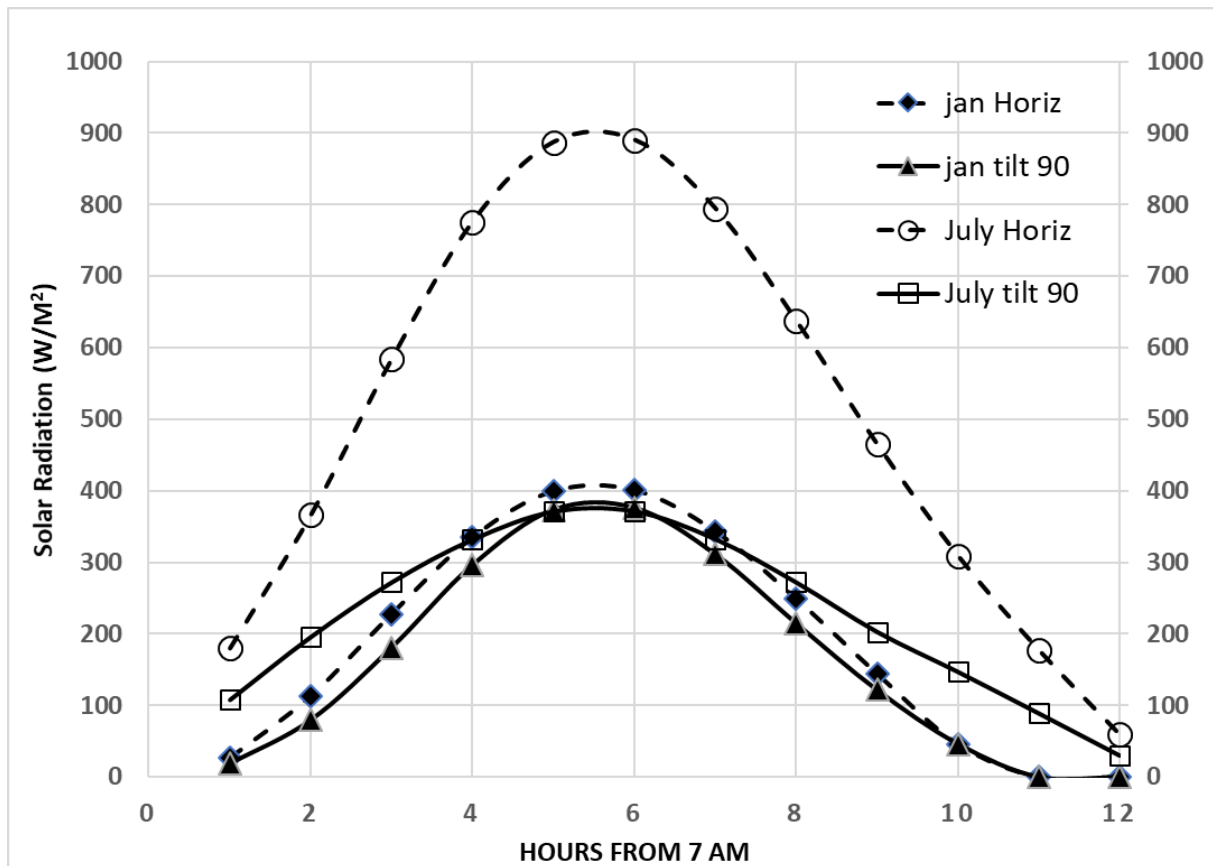


Figure 8. Summer and winter hourly radiation for horizontal and vertical surfaces in Beirut

5. Transient Thermal Analysis

The transient simulations and temperature analyses are performed using solar and climatic data corresponding to the average day of January and the average day of July, in order to capture representative winter and summer thermal behavior.

Initially, the modelling assumes two nodes across the hollow concrete block – an inner and an outer one. The relevant equations are derived to determine the temperature profiles generated. Beyond that, and to allow for two material components, the block is divided into two equal parts: one side is exposed to the sun and contains a transparent (or translucent) material (such as glass), and the other part is regular concrete. This configuration allows for the determination of temperatures at three distinct nodes.

5.1. HCB with Two Boundary Nodes

As an improved model allowing both heat conduction and heat storage effects, the pure standard HCB is considered to have two surface nodes, as shown in Fig. 9a.

The first/outer node of the HCB is exposed to solar radiation, absorbing energy from the sun. Neglecting reflection and assuming normal incidence, the HCB loses energy by convection to the surrounding air while also transferring heat internally to the second node by conduction. The balance between the absorbed solar energy, convective heat loss, and conductive heat transfer determines the temperature change of the first node over time. The second node of the HCB is assumed to lose energy through convection to the surrounding air (this assumes the HCB block is sitting individually in the ambient) and gain heat from the first node through conduction. Similarly, the balance between these heat transfers determines the temperature change of the second node over time.

The nodal equations for the opaque system in Fig. 9a are:

$$\alpha_{HCB}GA - h_oA(T_1 - T_a) - \frac{k_{HCB}A}{W}(T_1 - T_2) = \rho \frac{V}{2}C \frac{dT_1}{dt} \tag{35}$$

$$\frac{k_{HCB}A}{W}(T_1 - T_2) - h_iA(T_2 - T_a) = \rho \frac{V}{2}C \frac{dT_2}{dt} \tag{36}$$

where h_o is the outside coefficient of heat convection, h_i is the inside coefficient of heat convection, k_{HCB} is the thermal conductivity of the HCB, T_1 is the temperature of node 1, T_2 is the temperature of node 2, W is the width (m), ρ is the density of the concrete (kg/m^3), V is the volume of the concrete (m^3) assigned to each node and C is the specific heat of the HCB (J/kgK). Solving these two differential equations gives the transient temperature response for both winter and summer conditions, as shown in Figs. 10 and 11.

The two-node results in Fig. 10 show three basic features: firstly, the exterior half-slab temperature T_1 amplifies the solar forcing, rising from 10 °C at 7:30 AM to about 21.5 °C and peaking near 2:00 PM, roughly 4 °C above the ambient maximum of 18 °C at 12:30 PM. Secondly, the interior half-slab T_2 exhibits pronounced damping and delay, climbing more slowly to only 15.8 °C around 4:00 PM—fully three hours after the start of heating. Finally, the approximately 2–3 h phase lag and reduced amplitude of T_2 quantify the concrete’s thermal capacitance and conductive resistance, underscoring the block’s ability to attenuate and smooth diurnal temperature swings.

In July and as illustrated in Fig. 11, the two-node model shows the exterior half-slab temperature T_1 rising rapidly from 25 °C at 7:30 AM to about 38.8 °C by 2:30 PM—roughly 4 °C above the ambient peak of 35 °C at 12:45 PM. The interior half-slab T_2 responds more gradually, reaching only 33.2 °C around 5:00 PM. This ~3 h phase lag and reduced amplitude of T_2 quantify the concrete’s thermal capacitance and conduction resistance.

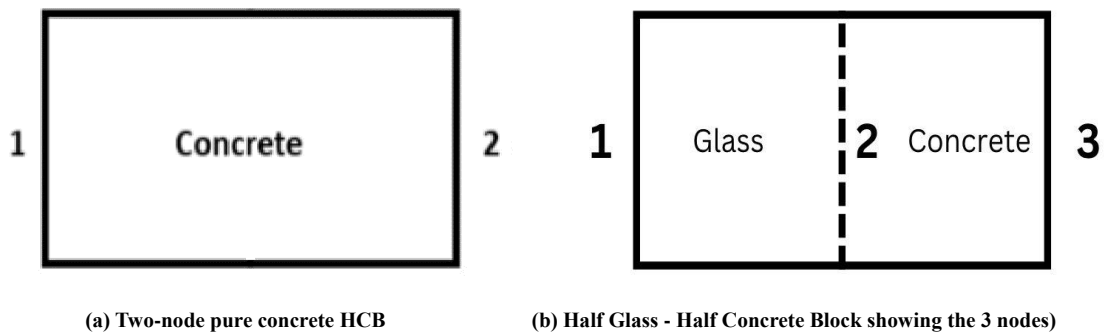


Figure 9. HCB 2 and 3 node models (node 1 is insulated)

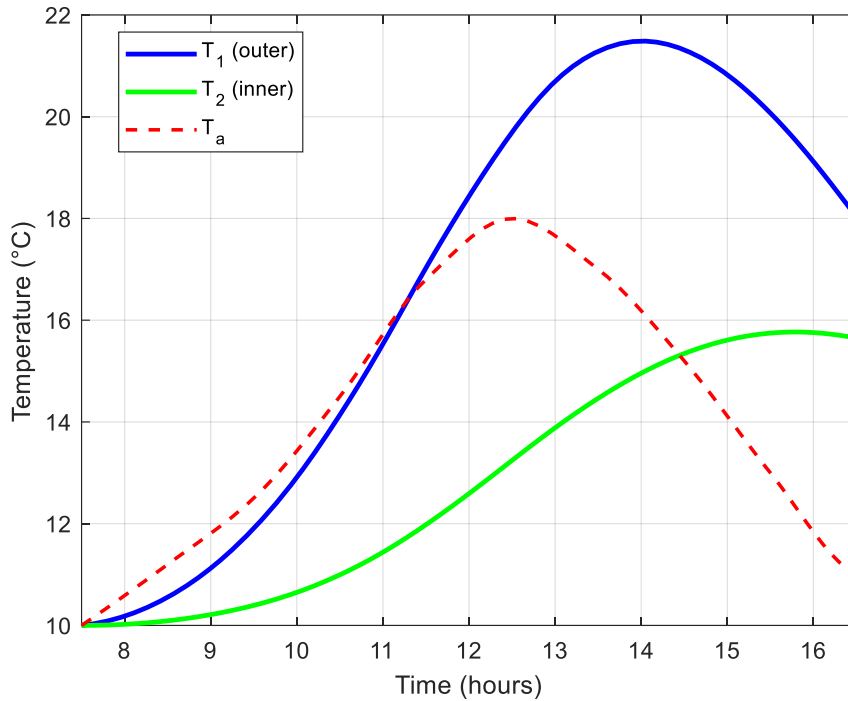


Figure 10. Temperature Distribution for HCB with Two Surface Nodes for January

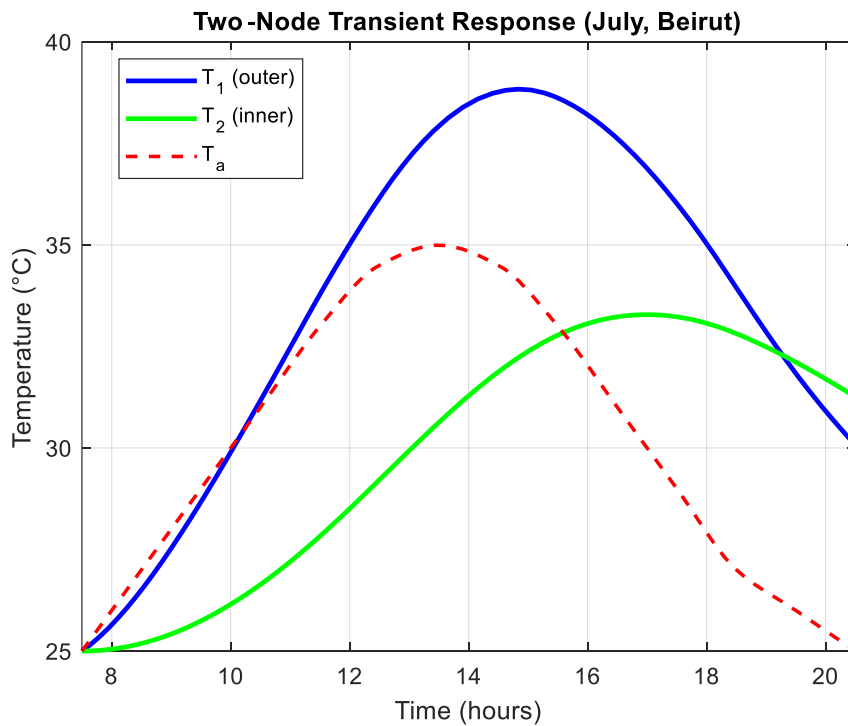


Figure 11. Temperature Distribution for HCB with Two Surface Nodes for July

5.2. Half Glass Half Concrete Block

The HCB is split into two equal sections: one made of transparent (or translucent) material (glass) and the other of regular concrete. With such a division, three nodes (2 surface and one interior) are treated instead of two surface nodes. The energy balance equations for the system shown

in Fig. 9b are:

$$\alpha_G GA - h_o A(T_1 - T_a) - \frac{k_G A}{W} (T_1 - T_2) = \rho_G A \frac{W}{4} C_G \frac{dT_1}{dt} \tag{37}$$

$$\tau_G(\alpha_G)GA + \frac{k_G A}{\frac{W}{2}}(T_1 - T_2) - \frac{k_C A}{\frac{W}{2}}(T_2 - T_3) = \bar{\rho}A\frac{W}{2}\bar{C}\frac{dT_2}{dt} \quad (38)$$

$$\frac{k_C A}{\frac{W}{2}}(T_2 - T_3) - h_i A(T_3 - T_a) = \rho_C A\frac{W}{4}C_C\frac{dT_3}{dt} \quad (39)$$

where α_G is the absorptivity of the glass, T_1 is the temperature of node 1, T_2 is the temperature of node 2, T_3 is the temperature of node 3, k_G is the thermal conductivity of glass, ρ_G is the density of glass, C_G is the specific heat of glass, τ_G is the transmissivity of glass assumed to be 0.95, $\bar{\rho}$ is an average of the two materials (concrete-glass) and is an approximation of the density at node 2, \bar{C} is an approximation of the specific heat at node 2, k_C is the thermal conductivity of concrete, ρ_C is the density of concrete, and C_C is the specific heat of concrete.

The first node, made of glass, is exposed to solar radiation, absorbing energy from the sun. It loses energy through convection to the surrounding air and also transfers heat to the second node (the interface between glass and concrete) through conduction. The balance between the absorbed solar energy, convective heat loss, and conductive heat transfer determines the temperature change of the first node over time. The second node receives solar energy transmitted through the glass, gains heat from the first node through conduction, and transfers heat to the third node (concrete) through conduction. The balance between these energy transfers absorbed solar energy, and conductive heat transfer from both the glass

and concrete parts determines the temperature change of the second node over time. The third node, made of concrete, gains heat from the second node through conduction and loses energy through convection to the surrounding air. The balance between the convective heat loss and the conductive heat gain from the second node determines the temperature change of the third node over time. Solving these three differential equations gives the transient temperature response for both winter and summer conditions, as shown in Figs. 12 and 13.

Fig. 12 shows the transient thermal behavior of the block throughout a clear January day in Beirut, where T_1 (blue) is the temperature of the outer glass surface, T_2 (green) is the temperature at the glass-concrete interface, and T_3 (magenta) is the inner concrete temperature, while T_a (red dashed) represents the ambient air temperature. The initial condition is taken as to be the 10 °C ambient at 6 a.m. As solar radiation increases, T_1 rises slightly due to absorbed solar energy but remains relatively low because of strong outward convection. The interface temperature T_2 rises sharply and reaches the highest value (about 26.7 °C) since it receives most of the transmitted solar energy. The inner concrete temperature T_3 increases quite slowly due to thermal resistance and high thermal mass, peaking later at around 21.6 °C. After midday, all temperatures begin to decline: T_1 cools quickly, T_2 retains heat the longest, and T_3 shows a delayed response. The ordering $T_2 > T_3 > T_1$ reflects the combined effects of solar gain, heat conduction, and thermal storage.

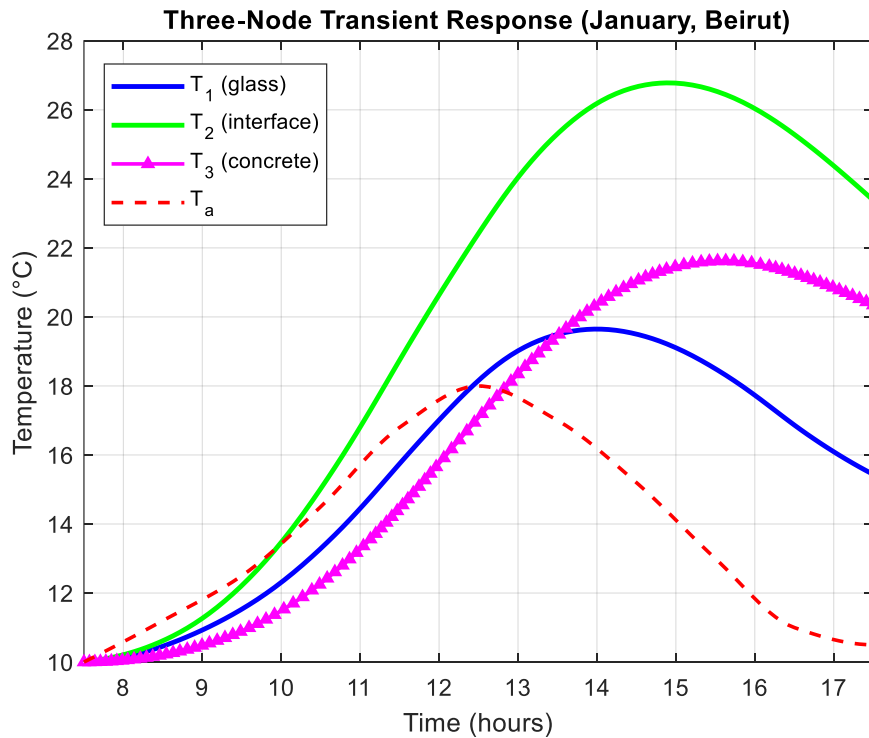


Figure 12. Half-Glass/Half-Concrete Temperatures for January

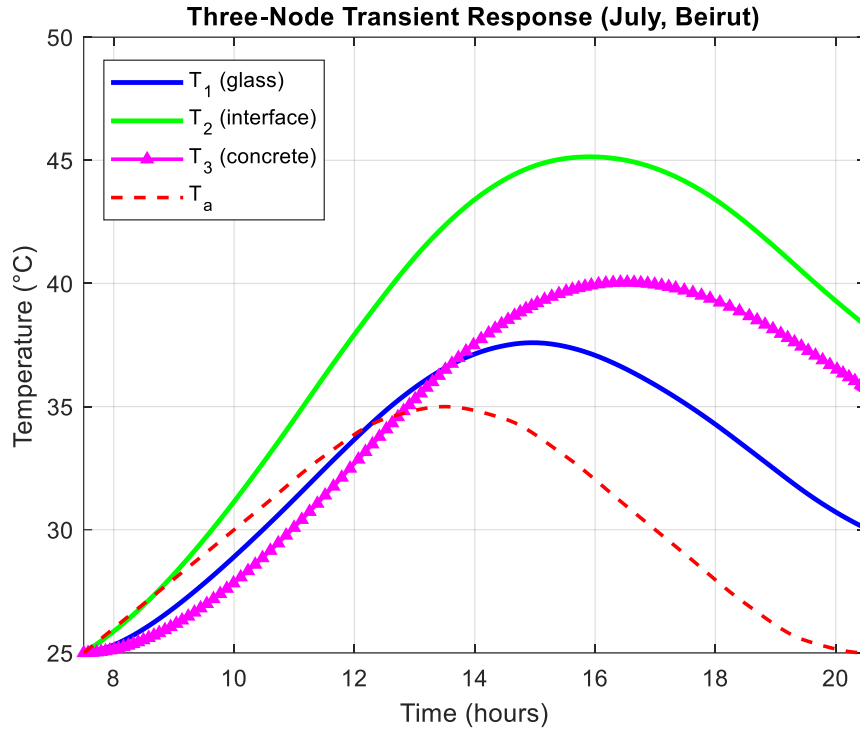


Figure 13. Half-Glass/Half-Concrete Temperatures for July

For the July case, as shown in Fig. 13, the overall temperature levels are significantly higher than in January due to higher ambient temperatures, although solar inputs are quite similar. The interface temperature T_2 peaks around 45.1 °C, while the concrete core T_3 reaches about 40 °C. Although the curve ordering $T_2 > T_3 > T_1$ after midday remains the same as for January, the peaks occur somewhat later in the day. These results confirm that in summer, the wall stores more heat and releases it more gradually due to the ambient temperature.

6. Generated Power

Since for the PVHCB, the HCB is to include a PV film at the gap (location of node 2 in the previous 3-node formulation). The PV film temperature will correspond to T_2 in the half-glass/half concrete model.

However, to highlight the difference between a traditional PV panel placed on a regular HCB of a walls outer sun-facing side and for a PVHCB in a built wall, the generated power per unit area is calculated for two cases: (1) when the outer node temperature is used as the PV cell temperature in the two-node case, and (2) when the interface node temperature is used in the three node case. The estimation is based on a temperature-dependent efficiency model formulated for crystalline silicon cells based on Skoplaki and Pavylos [19]:

$$\eta_p = 0.263 - 0.00048 T_p \quad (40)$$

where η_p is the effective power conversion efficiency, and T_p is the PV cell average temperature (in degrees Kelvin) and the corresponding power output is:

$$P_p = f \eta_p G \quad (41)$$

Here, G is the incident solar irradiance (in W/m^2) on the embedded PV film area, f is as previously defined and P_p is the resulting power output per unit area of the whole HCB. This gives the energy rate (in Watts) per unit PVHCB face area.

Based on Equation (41), the photovoltaic (PV) power output per unit area is calculated for both the two-node and three-node thermal models, evaluated for the months of January and July at a fixed air gap fraction $f = 0.5$ (see Fig. 14).

As shown in Fig. 14, the three-node model consistently predicts lower PV power output than the two-node model in both months, particularly around peak solar hours (12:00–14:00). This is due to the three-node model's enhanced ability to capture internal thermal resistances and more accurate PV cell temperature rise, leading to lower PV efficiency. Overall, the three-node model yields a more conservative and realistic estimate of PV performance, especially under summer conditions.

The PV output power per unit area, simulated using the three-node thermal model for three different gap length fractions ($f = 0.25, 0.5$ and 0.75), is presented in Fig. 15 for a typical day in January and in Fig. 16 for a typical day in July.

As shown in Fig. 15, increasing the gap length fraction (f) from 0.25 to 0.75 leads to a significant increase in PV

power output. This is primarily because a larger air gap fraction corresponds to a larger PV panel area integrated into the wall, thereby capturing more solar energy. At $f = 0.75$, the system reaches a peak power of around 65 W/m^2 compared to a low of 22 W/m^2 at $f = 0.25$. In addition to

increased surface area, the wider gap also helps improve thermal regulation, slightly reducing PV cell temperature and enhancing performance. The power curves for higher f -values are both taller and broader, indicating higher and more sustained energy production throughout the day.

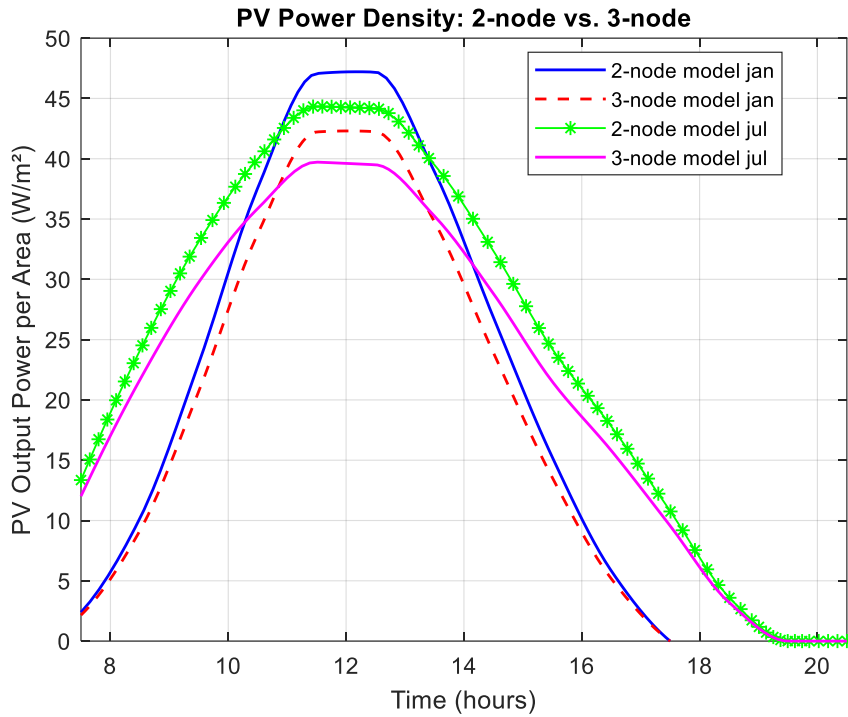


Figure 14. PV Output Power Per Unit Area for $f = 0.5$

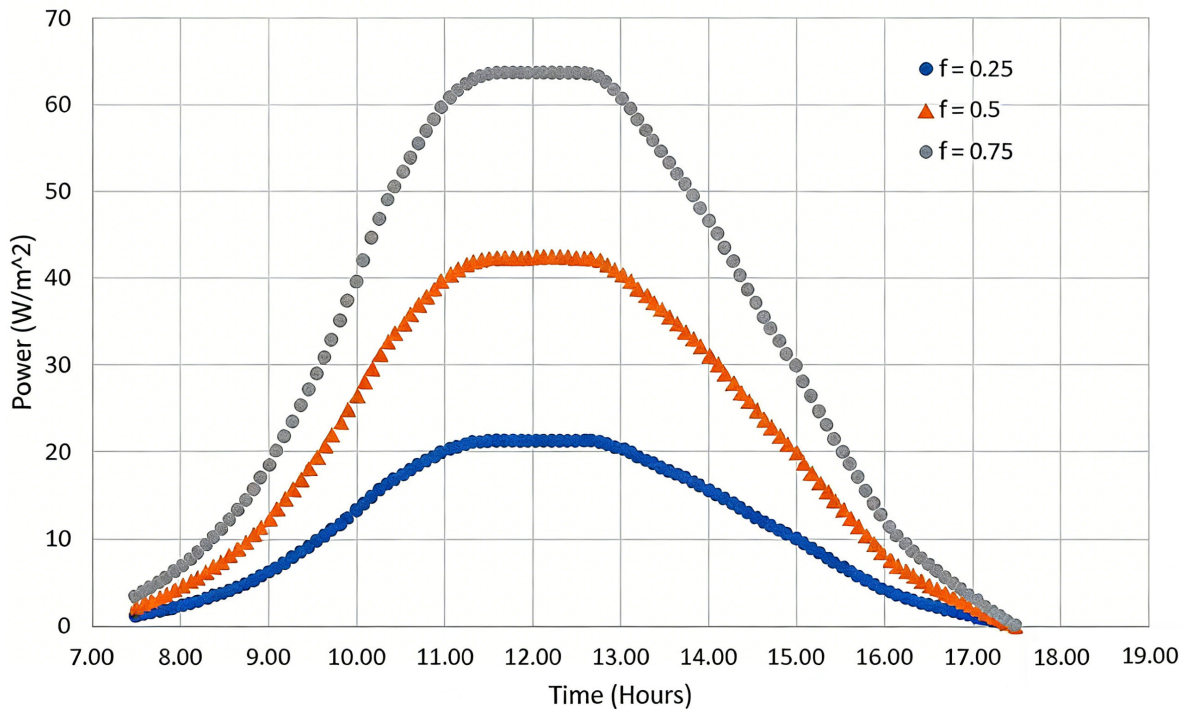


Figure 15. PVHCB January Power (3 node model)

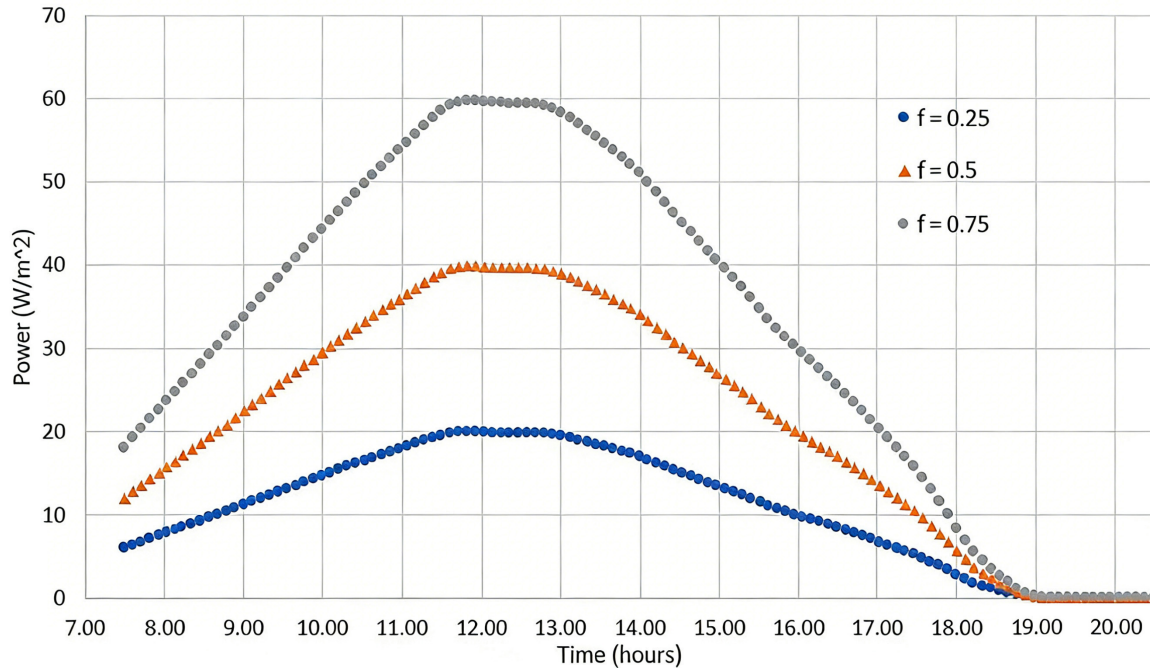


Figure 16. PVHCB July Power (3 node model)

In July and as illustrated in Fig. 16, increasing the gap length fraction f results in a clear improvement in power output. At $f = 0.75$, the system achieves a peak power of about 60 W/m^2 compared to roughly 20 W/m^2 at $f = 0.25$. This rise is largely due to the increase in PV area as the gap fraction grows, allowing more surface to absorb solar energy. Additionally, the longer daylight duration in July extends the generation window, particularly for larger values of f , which show wider and higher power curves. While higher temperatures in summer slightly reduce PV efficiency, the effect of increased absorbing area dominates, leading to greater total power output for larger gap fractions.

7. Conclusions

In addition to outlining a simple and accurate method for generating monthly and hourly solar energy data for any global region and applying the method to Beirut, Lebanon, this study's main contribution is the introduction of the Photovoltaic Hollow Concrete Block as a multifunctional building element that integrates thermal segregation and photovoltaic energy generation into a single structural unit. The block's dual-layer composition, featuring a translucent outer face and concrete inner core, enables both solar energy harvesting, as well as passive thermal regulation.

A series of parametric steady-state thermal resistance models was developed to investigate the influence of internal gap geometry and material composition on heat transfer. These models provided insight into optimizing U-values through variations in air gap length, width, and height. Subsequently, transient thermal simulations under

January and July climate profiles in Beirut enabled time-resolved temperature predictions for both two-node and three-node configurations. The results show that while the two-node model overestimates PV performance by using the surface temperature, the three-node model provides a more realistic estimate by considering internal temperature rise at the PV-glass/concrete interface.

Electrical performance evaluations show that increasing the air gap length fraction enhances the power output due to the corresponding increase in PV surface area. Despite higher summer temperatures, slightly reducing PV efficiency, July (representing typical summer conditions) yields higher total energy production due to extended daylight hours.

Additionally, the alignment of air channels across neighboring PVHCB units can significantly influence the cooling behavior via buoyancy-driven convection, thereby affecting PV temperature and performance. This suggests that block-to-block connectivity and wall assembly strategy are as critical as individual unit design.

On a $5 \times 4 \text{ m}^2$ small south-facing wall and at a normal insolation and incidence with $f = 0.5$, the maximum power generated on an average day of January is 846 W and the maximum power generated at an average day of July is 794 W . While the instantaneous peak is higher in January due to lower ambient temperatures and better PV efficiency, the total energy generation is greater in July owing to the longer daylight duration. These results assume that the outer PVHCB half is made from a highly transmissive material such as glass. In future work, beyond refining the model to account for bond or fastening materials in the PVHCB, translucent concrete—with expected transmissivities no greater than about

0.25—could be explored as an alternative outer layer. Although this would reduce power output, it may enhance the structural strength of the wall. A thorough technoeconomic feasibility assessment would be necessary to evaluate this approach. Additionally in a practical application, to ensure sufficient waterproofing of the exterior wall, a thin transparent polycarbonate endurance pane may be included.

In conclusion, the PVHCB represents a novel, modular, and sustainable approach to integrating renewable energy into the built environment. It unifies structural, thermal, and electrical building functions—offering a promising pathway for energy-positive building envelopes. Future research could focus on experimental validation of power output, technoeconomic studies of PVHCB-constructed

walls, determination of optical properties of existent, selection of block interface bonding materials and novel translucent materials, structural mechanics of PVHCB-constructed walls, and the architectural integration of such walls across diverse climatic zones.

Funding Statement

The author(s) received no specific funding for this study.

Conflicts of Interest

The authors declare that they have no conflicts of interest to report regarding the present study.

Appendix

Derivation of Equation 14

Central Gap Dimensions:

$$L_g = fL$$

$$W_g = gW$$

$$H_g = sH,$$

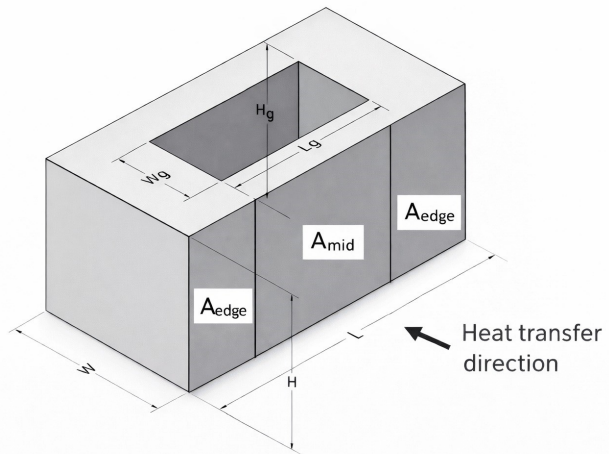
where f , g , and s are fractions.

Surface Areas for heat transfer:

$$A_{mid} = A_1 = L_g H_g = fLsH$$

$$A_{edge} = A_2 = \left(\frac{L - L_g}{2}\right)H = \left(\frac{L - fL}{2}\right)H$$

$$A_{total} = A_{mid} + 2A_{edge}$$



Thermal Resistances:

Middle Section:

Series resistances: Convection (outer) + Conduction in concrete + Pseudo Conduction in gap + Conduction in concrete + Convection (inside)

$$R_{mid} = \frac{1}{h_o A_1} + \frac{W - W_g}{2} \frac{1}{k_c A_1} + \frac{W_g}{k_g A_1} + \frac{W - W_g}{2} \frac{1}{k_c A_1} + \frac{1}{h_i A_1}$$

or:

$$R_{mid} = \frac{1}{h_o A_1} + \frac{W - W_g}{k_c A_1} + \frac{W_g}{k_g A_1} + \frac{1}{h_i A_1}$$

Taking a common denominator:

$$R_{mid} = \frac{k_c k_g h_i + (W - W_g) h_o k_g h_i + W_g h_o k_c h_i + h_o k_c k_g}{h_o k_c k_g h_i f L s H} \quad (\text{K/W})$$

Or as resistance per total exposed surface area ($\dot{Q} = A \frac{\Delta T}{\sum R + \sum \frac{1}{h}}$):

$$R_{mid} = \frac{A_{total} [k_c k_g h_i + (W - W_g) h_o k_g h_i + W_g h_o k_c h_i + h_o k_c k_g]}{h_o k_c k_g h_i f L s H} \quad (\text{m}^2 \text{K/W})$$

Let,

$$D_1 = k_c k_g h_i + (W - W_g) h_o k_g h_i + W_g h_o k_c h_i + h_o k_c k_g$$

$$\frac{1}{R_{mid}} = \frac{h_o k_c k_g h_i f L S H}{A_{total} D_1}$$

Edge Section:

Series resistances: Convection (outer) + Conduction in concrete + Convection (inside)

$$R_{edge} = \frac{1}{h_o A_2} + \frac{W}{k_c A_2} + \frac{1}{h_i A_2}$$

$$R_{edge} = \frac{1}{h_o \frac{(L-fL)H}{2}} + \frac{W}{k_c \frac{(L-fL)H}{2}} + \frac{1}{h_i \frac{(L-fL)H}{2}}$$

Taking common denominator:

$$R_{edge} = \frac{2k_c h_i + 2W h_o h_i + 2h_o k_c}{h_o k_c h_i (L-fL)H} \text{ (K/W)}$$

Or as resistance per total exposed surface area

$$R_{edge} = \frac{A_{total} [2k_c h_i + 2W h_o h_i + 2h_o k_c]}{h_o k_c h_i (L-fL)H} \text{ (m}^2\text{K/W)}$$

Let,

$$D_2 = 2k_c h_i + 2W h_o h_i + 2h_o k_c$$

The mid-section is in thermal parallel with the two edge sections:

$$\frac{1}{R_{total}} = \frac{1}{R_{mid}} + \frac{2}{R_{edge}}$$

Where from above:

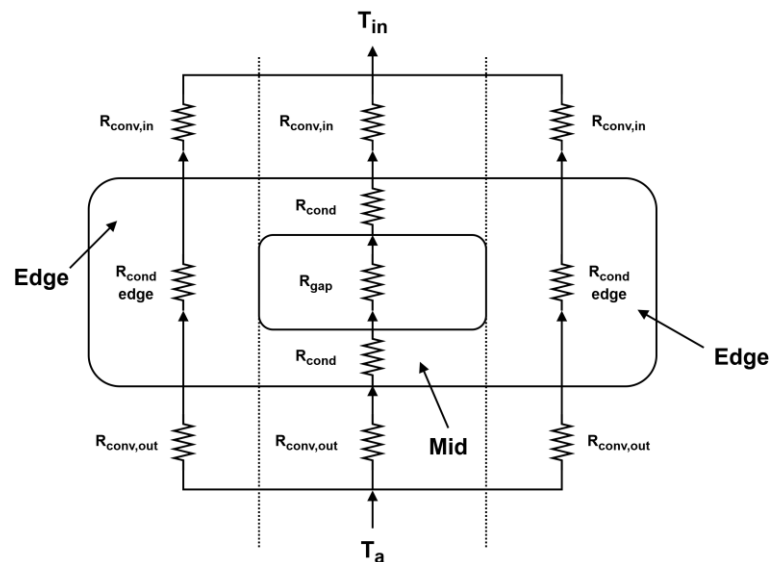
$$\frac{2}{R_{edge}} = \frac{2h_o k_c h_i (L-fL)H}{A_{total} D_2}$$

Therefore:

$$\frac{1}{R_{total}} = \frac{h_o k_c k_g h_i f L S H}{A_{total} D_1} + \frac{2h_o k_c h_i (L-fL)H}{A_{total} D_2}$$

Giving:

$$U_{total} = \frac{h_o k_c h_i (k_g f L S H D_2 + 2(L-fL)H D_1)}{A_{total} D_1 D_2}$$



REFERENCES

- [1] Okirigiti M.O., Kim C.M., Choi H., Alluri N.R., Park K., "Recent advances in Thermoelectric materials and devices: Improving power generation performance," *J. Powder Materials*, vol. 32, no. 1, pp. 1-15, 2025. DOI: 10.4150/jpm.2024.00395.
- [2] Jabri M., Masoumi S., Sajadirad F., West R., Pakdel A., "Thermoelectric energy conversion in buildings," *J. Materials Today Energy*, vol 32, pp. 1-21, 2023. DOI: 10.1016/j.mtener.2023.101257.
- [3] Wehbe M., Dgheim J., Sassine E., "Thermoelectric Phenomenon in hollow blocks," *Condensed Matter*, 2021. DOI: 10.48550/arXiv.2108.07228.
- [4] Bevilacqua P., Bruno R., Szyska J., Cirone D., Rollo A., "Summer and winter performance of an innovative concept of Trombe wall for residents of buildings," *Energy*, vol. 258, p. 124798, 2022. DOI: 10.1016/j.energy.2022.124798.
- [5] Sirin C., Goggins J., Hadjukiewicz M. A., "Review on Building-Integrated Photovoltaic Systems for Green Buildings," *Appl. Therm. Eng.*, vol. 229, no. 9, 2023. DOI: 10.1016/j.applthermaleng.2023.120607.
- [6] Liu R., Wentao D., Guoqing H., Qikun W., "Development of Wall-integrated Solar Energy Technologies," *Energies*, vol. 18, no. 4, 2025. DOI: 10.3390/en18040952.

- [7] Ma X, Ghosh A., and Saboor S., "Building integrated photovoltaic-thermal systems (BIPVT) and spectral splitting technology," *Next Sustainability*, vol. 4, p. 100056, 2024. DOI: 10.1016/j.nxsust.2024.100056.
- [8] Fischer A., "Mitrex releases the Solar Brick—a solar-integrated building facade.," March 4 2022, *PV Magazine USA*. <https://pv-magazine-usa.com/2022/03/04/mMitrex> (accessed September 18, 2025)
- [9] Shukla A.K., Sudhakar P. and Baredar P. A., "Comprehensive review on design of building integrated photovoltaic system," *Energy and Buildings*, vol. 128, pp 99-110, 2016. DOI: 10.1016/j.enbuild.2016.114867.
- [10] Belloni E., Bianchini G., Casini, M., Faba, A., Intravaia M., Audani A., Lozito G.M., "An overview on building-integrated photovoltaics: technological solutions, modeling, and control," *Energy and Buildings*, vol. 324, pp. 1-15, 2024. DOI: 10.1016/j.enbuild.2024.114867.
- [11] Jelle B.P., "The path to the building integrated photovoltaics of tomorrow," *Energy Procedia*, vol. 20, pp. 78-87, 2012. DOI: 10.1016/j.egypro.2012.03.010.
- [12] Skandalos N., Kapsalis V., Karamanis D., "The effect of local climatic conditions on the building integration of photovoltaics," in *Proc. 3rd Int. Conf. Environmental Design (ICED2022)*, Athens, Greece, Oct. 22–23, 2022, vol. 1123, Art. no. 012020, DOI: 10.1088/1755-1315/1123/1/012020.
- [13] Elghezanwy D., and Eltarabily S., "A Review of Translucent Concrete as a New Innovative Material in Architecture," *Civil Engineering and Architecture*, vol. 8, no. 4, pp. 571-579, 2020. DOI: 10.13189/cea.2020.080421.
- [14] Sassine E., Cherif Y., Dgheim J. and Antezak E., "Experimental and numerical thermal assessment of lebanese traditional hollow blocks," *Int. J. Thermophys.*, vol. 41, pp. 1-21. DOI: 10.1007/s10765-020-02626-7.
- [15] Cengel Y.A., "Steady Heat Conduction," In *Heat Transfer, A Practical Approach*, Chapter 3, 2nd ed, McGraw-Hill, 2006, pp. 131-218.
- [16] Moucharrafié F., Farah E., Nuwayhid R., Nehme B., "Improving the Thermal Performance of External Wall in Common Construction Practice in Lebanon," *Civil Engineering and Architecture*, vol. 12, no. 4, pp. 2731-2743, 2024. DOI: 10.13189/cea.2024.120417.
- [17] Duffie JA., Beckman WA., "Available Solar Radiation," In *Solar Engineering of Thermal Processes*, Chapter 2, 4th ed. Hoboken, NJ, USA: Wiley, 2013.
- [18] European Commission, Joint Research Centre, *PVGIS: Photovoltaic Geographical Information System*. [Online]. Available:https://joint-research-centre.ec.europa.eu/pvgis_en, Accessed: April 3, 2025.
- [19] Skoplaki E. and Palyvos J., "On the temperature dependence of photovoltaic module electrical performance: a review of efficiency/power correlations," *Solar Energy*, vol. 83, pp. 614–624, 2008. DOI: 10.1016/j.solener.2008.10.008.